DOI: 10.1002/ ((please add manuscript number))

Full paper

Design of Hierarchical Ni-Co@Ni-Co Layered Double Hydroxide Core-Shell Structured Nanotube Array for High-Performance Flexible All-Solid-State Battery-type Supercapacitors

*Yan Liu, Nianqing Fu, Guoge Zhang, Ming Xu, Wei Lu, Limin Zhou, Haitao Huang**

Y. Liu, Dr. N. Q. Fu, M. Xu, Prof. H. Huang

Department of Applied Physics, The Hong Kong Polytechnic University, Hung Hom, Kowloon, Hong Kong, China.

E-mail address: aphhuang@polyu.edu.hk

Dr. W. Lu

University Research Facility in Materials Characterization and Device Fabrication, The Hong Kong Polytechnic University, Hong Kong, China.

Prof. G. Zhang

School of Materials Science and Engineering, South China University of Technology, Guangzhou, 510640, P. R. China

Prof. L. Zhou

Department of Mechanical Engineering, The Hong Kong Polytechnic University, Hung Hom, Kowloon, Hong Kong, China

Keywords: Hierarchical porous nanotubes; Electrode; Ni-Co@Ni-Co LDH core-shell structure; Battery-type supercapacitor.

A novel hierarchical nanotube array (NTA) with a massive layered top and discretely separated nanotubes in a core-shell structure, i.e., nickel-cobalt metallic core and nickel-cobalt layered double hydroxide shell (Ni-Co@Ni-Co LDH) was grown on carbon fiber cloth (CFC) by template-assisted electrodeposition for high-performance supercapacitor application. The synthesized Ni-Co@Ni-Co LDH NTAs/CFC showed high capacitance of 2200 F g^{-1} at a current density of 5 A g^{-1}, while 98.8% of its initial capacitance was retained after 5,000 cycles. When the current density was increased from 1 to 20 A g^{-1}, the capacitance loss was less than 20%, demonstrating excellent rate capability. A highly flexible all-solid-state battery-type supercapacitor was successfully fabricated with Ni-Co LDH NTAs/CFC as the positive electrode and electrospun carbon fibers/CFC as the negative electrode, showing a maximum specific capacitance of 319 F g^{-1}, a high energy density of 100 W h kg^{-1} at 1.5 kW kg^{-1}, and good cycling stability (98.6% after 3,000 cycles). These fascinating electrochemical properties were resulted from the novel structure of electrode materials and synergistic contributions from the two electrodes, showing great potential for energy storage applications.

1. Introduction

As one of the most promising types of energy storage devices, supercapacitors have been applied in many fields, such as back-up power systems, electric vehicles and portable electronic devices,[1] because of their high power density and long cycle life. There are two types of supercapacitors based on energy storage mechanism, i.e., electric double-layer capacitors (EDLCs) and pseudocapacitors. EDLCs are primarily prepared by carbon-based materials such as carbon nanotubes (CNTs),[2] activated carbon (AC)[3] and

graphene.[4] This type of supercapacitor stores energy by electrostatic accumulation of charges in the electric double-layer. Due to the high cycling stability and low-cost benefit, EDLCs are widely used in commercial capacitors. However, the specific capacitance is relatively low for EDLCs, which limits their further applications. In pseudocapacitors, transition metal oxides/hydroxides (HD) and polymers, e.g., RuO_2,[5] MnO_2,[6] Co_3O_4,[7] $Ni(OH)_2$,[8] $Co(OH)_2$,[9] polyaniline,[10] and polypyrrole[11] are normally used as electrode materials to provide higher specific capacitance than EDLCs do. Among them, $Ni(OH)_2$, particularly, is considered promising due to its high theoretical battery-type specific capacitance (2082 F g^{-1}),[8a] low-cost and high redox activity. However, its rate capability is greatly limited by the low electric conductivity (~10^{-5} to 10^{-9} S cm^{-1}). Thus, it is still challenging to fabricate $Ni(OH)_2$-based battery-type supercapacitors with high rate capability.

In recent years, much efforts were devoted to performance improvement of $Ni(OH)_2$-based battery-type supercapacitors.[12] One strategy is to use highly conductive carbon materials (AC, CNTs, and graphene, etc.) as the backbone to support $Ni(OH)_2$, which enhances the rate capability by shortening the electron transport distance.[12f] For example, Wei *et al*.[13] prepared hierarchical flowerlike $Ni(OH)_2$ on graphene sheets, which showed a specific capacitance of 1735 F g^{-1}. However, the strong π-π interactions and the van der Waals force between the graphene platelets resulted in the agglomeration of graphene sheets, and the decoration of $Ni(OH)_2$ on graphene was not homogeneous. These problems can be overcome effectively by partially substituting Ni^{2+} with certain cations, such as Co, Al, Mn and Fe. Ni-Co hydroxides show enhanced capacitance and cycle life as compared with pure $Ni(OH)_2$. Wu *et al*.[14] reported that the layered Ni-Co

double hydroxide hybrid film displayed a significantly high gravimetric capacitance of 2682 F g^{-1} at 3A g^{-1}, but the capacitance faded rapidly to 1706 F g^{-1} when the current density was increased to 20 A g^{-1}. Liu *et al*.[15] described an accumulative approach to the synthesis of Ni-Co double hydroxides/graphene binary composite by a co-precipitation process. The composite showed high specific capacitance (2360 F g^{-1} at 0.5 A g^{-1}) and excellent rate capability (capacitance retention ~86% as the current density increased to 20 A g^{-1}). However, the cycling stability was relatively poor (~25% decay after 5,000 cycles). Hence, it is still desirable to develop strategies to produce electrode materials with high specific capacitance and good rate capability, as well as long cycle life.

Conventional supercapacitors using liquid electrolyte [16] may have the leakage problem. Recently, all-solid-state supercapacitors based on carbon fiber cloth (CFC) with high specific surface area and good conductivity have attracted considerable attention due to the flexibility, wearability, safety, and low cost of CFC. However, these flexible all-solid-state supercapacitors still display low capacitance and low energy density.[17] It remains challenging while highly desirable to obtain flexible all-solid-state supercapacitors with high performance.

Nanotube arrays (NTAs) with well-defined pore structures have recently drawn great attention in the design of electrode materials due to the high surface area. It has been demonstrated that the well-oriented NTAs also contribute to the ion diffusion and substantially facilitate the electrolyte penetration.[18] Li *et al* [19] reported Ni@NiO core/shell nanoparticle tube arrays fabricated by sacrificial ZnO nanorods template. However, most of the NTAs reported had closely packed nanotubes (without top) only,[20] which result in low surface area, low number of electrochemical active sites, and difficult

electrolyte infiltration. Besides, it is usually difficult to fabricate metal@metal oxide or hydroxide core/shell structure by one-step electrodeposition.[21] For example, $NiCo_2S_4$@$Co(OH)_2$ core/shell nanotube arrays have to be fabricated by a two-step hydrothermal reaction and electrodeposition method.[22] A novel 3D core/shell structured Co_3O_4@$Ni(OH)_2$ has to be fabricated by hydrothermal reaction, followed by a chemical bath deposition.[23] Recently, we developed a simple and efficient electrodeposition in a source-free electrolyte to fabricate Ni@NiO core/shell dendrites,[24] which paved the way for the simple synthesis of metal@metal oxide or hydroxide core/shell structures.

Herein, we used low-cost and environment-friendly ZnO nanorod arrays (ZnO NRAs) grown on CFC as a template to design and fabricate Ni-Co@Ni-Co LDH NTAs (core-shell structured) with separated tubes and hierarchical top for efficient utilization of high surface area (**Scheme 1**). The well-aligned Ni-Co@Ni-Co LDH NTAs designed in this work represent a new example of nanostructure engineering for better electrochemical performance, owing to the following features: (i) the Ni/Co metallic core provides a pathway for efficient charge transport, which effectively overcomes the weakness of Ni-Co LDH (relatively poor conductivity); (ii) the binary metal ions of Ni^{2+}/Ni^{3+} and Co^{2+}/Co^{3+} enhance capacitive properties since the mixed valence states can increase the number of active sites to trigger more redox reactions; (iii) the nanotube structure with a hierarchical top in addition to the separated tubes not only facilitates the transport of ions, but also provides numerous electrochemical reaction sites; (iv) well-aligned NTAs growing homogenously on the CFC current collector enable almost all the nanotubes to participate in the electrochemical reactions without any dead volume. In a liquid-electrolyte-based three-electrode test, Ni-Co@Ni-Co LDH NTAs/CFC achieved a

very high specific capacitance of 2414 F g^{-1}, in 1 mol L^{-1} NaOH aqueous solution. An all-solid-state flexible battery-type supercapacitor (FBSC) was assembled using Ni-Co@Ni-Co LDH NTAs/CFC as the positive electrode and CNFs/CFC as the negative electrode. The as-fabricated FBSC exhibited a fascinating electrochemical performance with the maximum specific capacitance of 319 F g^{-1}, high energy density of 100 W h kg^{-1} at a power density of 1.5 kW kg^{-1}, and good cycling stability (98.6% capacitance retention rate after 3,000 cycles). Our work reported here sheds light on the effective structural engineering of electrodes to improve electrochemical performance of energy storage devices.

2. Results and Discussion

2.1 Positive Electrode Materials

In this work, CFC was used both as the current collector and the support for active materials. Figure S1 (Supporting Information) shows that CFC is composed of many carbon fibers with diameters of about 8 μm. For the electrochemical deposition of ZnO NRAs, only at a current density of 0.8 mA cm^{-2} were dense, homogeneous, and vertically aligned ZnO NRAs formed with a separation around 100-500 nm among NRAs (**Figure 1**a and 1b). ZnO NRAs electrodeposited at a too low or a too high current density are shown in Figure S2a and S2b (Supporting Information). The diameter and length of ZnO NRAs are about 500 nm and 2 μm, respectively (Figure S3, Supporting Information). From the HRTEM image and SAED pattern, the growth direction of ZnO NRA is determined to be along [001] direction, the polar *c*-axis of ZnO crystals.[25] After the second electrodeposition, nickel and cobalt hydroxides were coated on the surfaces of ZnO NRAs. Similarly, only at a current density of 4 mA cm^{-2} can hierarchical Ni-

Co@Ni-Co LDHs be conformally deposited on ZnO NRAs, with nanorods clearly separated to each other (Figure 1c and 1d), as compared with those deposited at a too low (1 mA cm^{-2}) or a too high (6 mA cm^{-2}) current density (Figure S2c and S2d, Supporting Information). High magnification SEM image (Figure 1e) clearly shows that the Ni-Co@Ni-Co LDH NR looks like a fungus composed of a big top and a small body (marked by rectangles in Fig.1e). The big top is made of layered sheets (Figure 1f) which greatly enhance the specific surface area of the active material. After dissolving the ZnO NRAs template, Ni-Co@Ni-Co LDH NTAs/CFC was fabricated (Figure S4, Supporting Information). The morphologies of the Ni-Co LDH NTAs of different Ni:Co ratios (unless otherwise specified, all the Ni:Co ratio mentioned hereafter refers to the molar ratio of Ni:Co in the electrolyte for electrodeposition) are similar to each other (Figure S4, S5a**,** S5c, and S5e, Supporting Information), with the nanotubes standing vertically and separated apart from each other. Exceptionally, the Ni-Co@Ni-Co LDH NTAs (Ni:Co=0:10) were composed of larger plates and the nanotube structure was completely destroyed (Figure S5g, Supporting Information). This may be attributed to the fast electrodeposition of Co element. In general, as the content of cobalt was increased gradually, the coated Ni-Co@Ni-Co LDHs became more net-like until it appeared flaky. The chemical composition of Ni-Co@Ni-Co LDH NTAs/CFC is analyzed by EDX as shown in Table S1. The compositions are absolutely different from the starting feeding molar ratios of Ni:Co. This is expected and is due to different reaction resistances present in the solution (e.g. surface overpotential, concentration overpotential, and ohmic overpotential, etc.).[26] The deposition of Co is always preferred due to its dominant electrochemical activity at 4 mA cm^{-2}.

Figure 2a shows that the top of the Ni-Co@Ni-Co LDH NT (Ni:Co=5:5) has a diameter of ~700 nm and consists of many nanosheets, while the body of NT has a diameter of ~550 nm and consists of nanocrystals (20-30 nm in size). The body of NT has a wall thickness of ~50 nm. The nanosheets on the top of the NT provide a large amount of active sites for electrochemical reaction and the void space between neighboring NTs is beneficial for electrolyte infiltration and ion diffusion without any blocks. HRTEM image of the Ni-Co@Ni-Co LDH NTA (Figure 2b) shows the lattice fringes corresponding to the (111) plane of nickel or (002) plane of cobalt and the (113) plane of α-$Ni(OH)_2$ or α-$Co(OH)_2$. The selected-area electron diffraction (SAED) pattern (inset of Figure 2b) reveals that the body of the Ni-Co@Ni-Co LDH NTA consists of many nanocrystals. The diffraction rings match the planes of Ni (or Co) and α-$Ni(OH)_2$ (or α-$Co(OH)_2$). EDX mapping (Figure 2d-2f) shows that Ni, Co and O are well-dispersed and homogeneously mixed in the NTA. It is worth noting that Ni:Co:O ratio in the Ni-Co@Ni-Co LDH NTAs (Ni:Co=5:5) is around 1:3.4:1.8 (Table S1, Supporting Information), deviating from the stoichiometric ratio of $Ni(OH)_2$ (or $Co(OH)_2$) and implying the existence of metallic nickel and cobalt, in agreement with the SAED result. The top of the NTA is made up of the Ni-Co@Ni-Co LDH nanosheets (Figure S6, Supporting Information), whose SAED pattern is similar to that of the body (Figure 2). EDS also confirms the elemental composition of Ni, Co, and O (Figure S7).

Figure 3a shows that Ni-Co@Ni-Co LDH NTAs/CFC (of different Ni:Co ratios) contains hexagonal cobalt with a space group of P63/mmc (JCPDS Card No. 05-0727) and cubic nickel with a space group of $Fm\bar{3}m$ (JCPDS Card No. 04-0850), apart from CFC (JCPDS Card No.41-1487).[12f] The characteristic diffraction peak observed around

44.5° is caused by the overlap of the (111) peak from nickel and the (002) peak from cobalt. A wide diffraction peak at around 11.3° in the Ni-Co@Ni-Co LDH NTAs/CFC (Ni:Co=5:5) can be indexed as (003) plane of α-$Ni(OH)_2$ or α-$Co(OH)_2$ (hydrotalcite-like LDH phase).[14] However, no obvious peaks of hydrotalcite-like LDH phase are found in the samples with other Ni:Co ratio, implying their tiny crystals. Meanwhile, the disappearance of ZnO peaks in the Ni-Co@Ni-Co LDH NTAs/CFC indicates that the ZnO NRA template was completely removed by alkaline solution.

Figure 3b displays that Ni-Co@Ni-Co LDH NTAs/CFC (Ni:Co=0:10) has the characteristic Raman peaks at 681, 612, 515, 473, and 191 cm^{-1}, corresponding to the A_{1g}, $F_{2g}(1)$, $F_{2g}(2)$, E_g, and F_{2g} modes of $Co(OH)_2$, respectively.[27] Ni-Co@Ni-Co LDH NTAs/CFC (Ni:Co=10:0) shows weak Raman activity and a wide band at 540 cm^{-1} (corresponding to $Ni(OH)_2$), suggesting its low crystalline.[27b] The result is in good agreement with its XRD pattern which reveals no extra peaks other than those of Ni metal. Two Raman peaks of Ni-Co@Ni-Co LDH NTAs/CFC (Ni:Co=3:7, 5:5, and 7:3) located at 473 and 515 cm^{-1} correspond to Ni-OH/Co-OH and Ni-O/Co-O (A_g) stretching modes, respectively.[26,27b,28] The characteristic peak at 182 cm^{-1} belongs to the LDH phase.[29] The Raman band at 681 cm^{-1} was observed to red shift with increasing amount of nickel in Ni-Co@Ni-Co LDH NTAs/CFC. The redshift of the A_{1g} Raman mode is probably due to tensile strain associated with Ni doping into the $Co(OH)_2$ lattice.[30] However, the band at 515 cm^{-1} blue shifts with increasing amount of nickel, similar to the observations of Bockman *et al*.[31] The change of the E_g Raman mode can be ascribed to the increase of lattice distortion and defects induced by nonstoichiometry due to the formation of the LDH phase.[30,32] Moreover, the shifted peaks became broadened. The peak

corresponding to ZnO (437 cm^{-1}) was not found in the samples, indicating the complete removal of ZnO, in agreement with XRD results.

To further study the composition of the electrode material, Ni-Co@Ni-Co LDH NTAs/CFC (Ni:Co=5:5) is characterized by X-ray photoelectron spectroscopy (XPS). Ni 2p XPS spectrum (**Figure 4**a) shows two kinds of nickel species, where the two spin-orbit doublets at 873.8 and 855.6 eV correspond to Ni $2p_{1/2}$ and Ni $2p_{3/2}$ signals of Ni^{2+}, while those at 874.9 and 856.9 eV can be ascribed to Ni $2p_{1/2}$ and Ni $2p_{3/2}$ signals of Ni^{3+}.[14,33] In Co 2p XPS spectrum (Figure 4b), two main spin-orbit lines and weak satellite signals (indicated as "Sat.") could be observed, suggesting the coexistence of Co^{2+} and Co^{3+} in the Ni-Co@Ni-Co LDH NTAs/CFC.[14,34] The fitting peaks at 797.5 and 782.1 eV are attributed to Co $2p_{1/2}$ and Co $2p_{3/2}$ signals of Co^{2+}. The peaks at 795.4 and 780.5 eV are ascribed to Co $2p_{1/2}$ and Co $2p_{3/2}$ signals of Co^{3+}. However, no signals of Ni or Co can be detected in the XPS spectra, although they can be observed in the XRD pattern. Considering that XPS is a surface sensitive technique, this result indicates that the Ni-Co@Ni-Co LDH NTAs/CFC may have a core-shell structure with the metallic Ni/Co as the core and the Ni-Co LDHs as the shell. XPS depth profiles of Ni 2p (Figure 4c) and Co 2p (Figure 4d) show a gradual increase in the amount of metallic Ni/Co with increasing etch depth, along with a gradual decrease in O content (Figure S8), which is supportive to the Ni/Co core and Ni-Co LDH shell structure. The formation of Ni-Co@Ni-Co LDHs core/shell structure can be explained by the two-stage electrochemical reaction. At the initial stage, due to the high concentration of Ni^{2+} and Co^{2+} in the SO_4^{2-}-containing electrolyte, metallic Ni and Co are preferentially deposited on the cathode, $Ni^{2+}/Co^{2+} + 2e^- \rightarrow Ni/Co$. As water is gradually electrolyzed ($2H_2O + 2e^- \rightarrow H_2 +$

$2OH^-$ *and* $O_2 + 2H_2O + 4e^- \rightarrow 4OH^-$), the local pH value increases and the surface of the electrode is gradually passivated, forming a layer of hydroxide, $Ni^{2+}/Co^{2+} + 2OH^- \rightarrow Ni(OH)_2/Co(OH)_2$, to cover the Ni and Co metal core. Thus, the Ni-Co and Ni-Co LDH core/shell structure was finally formed. This metallic core-semiconductor shell structure is beneficial to the electron collection and charge transport in the electrode. The rate capability is thus expected to be enhanced due to the fast charge/discharge kinetics.

Figure 5a and Figure S9 (Supporting Information) show typical cyclic voltammetry (CV) curves of Ni-Co@Ni-Co LDH NTAs/CFC at scan rates from 5 to 100 mV s^{-1}. All CV curves exhibited a strong pair of well-defined redox peaks, corresponding to the Faradaic reaction related to Ni(Co)-OH/Ni(Co)-O-OH (Equation 1-3, Supporting Information).[35] One pair of redox peaks in CV is observed due to the well mixing of Ni and Co ions in the hybrid by electrochemical deposition, as revealed by the EDS mapping results. Comparison of the CV reduction peak area suggests that the sample with Ni:Co=5:5 possesses the highest specific capacitance. Besides, the sample fabricated without ZnO NRA template (Ni-Co@Ni-Co LDHs/CFC) shows very poor pseudocapacitance (inset of Figure 5a) due to its collapsed structure (Figure S10, Supporting Information) with a compact layer of material covering CFC, which is detrimental to electrochemical performance. Therefore, the use of ZnO NRA template is necessary to effectively improve the electrochemical performance of the Ni-Co@Ni-Co LDHs. It is worth noting that the Ni-Co@Ni-Co LDH NTAs/CFC exhibits a single pair of redox peaks (Figure 5b and S9, Supporting Information) that shift with composition. The oxidation peak potential (*vs*. SCE) shifts to higher value with increasing amount of

Ni, in agreement with previous reports.[12f,15,35a] Importantly, the maximum redox peak current is found in the sample with Ni:Co=5:5, due to a possible synergistic effect.

Figure 5c and S11 (Supporting Information) show symmetric galvanostatic charge/discharge (GCD) curves of the Ni-Co@Ni-Co LDH NTAs/CFC, indicating excellent reversible redox reactions. The specific capacitance of an electrode was calculated by $C = \frac{I\Delta t}{S\Delta V}$, where I is the current density (A), Δt is the discharge time (s), S is the mass of active material (g), and ΔV is the potential window (V). The gravimetric capacitances of the Ni-Co@Ni-Co LDH NTAs/CFC at a current density of 5 A g^{-1} are determined to be 120, 1130, 2200, 819, and 609 F g^{-1} for the Ni:Co ratio of 0:10, 3:7, 5:5, 7:3, and 10:0, respectively. Obviously, the sample with Ni:Co=5:5 shows the highest capacitance (Figure 5d), consistent with the CV results. The above results show that the electrochemical performance of the sample depends on a proper amount of Ni and Co, which is also reflected in the gradual changes of crystal structure and morphology of the hybrid as a function of Ni:Co ratio. As shown in Figure 5e, the sample with Ni:Co=5:5 demonstrates the highest specific capacitance at all the current densities, which decreases from 2414 to 1980 F g^{-1} when the current density is increased from 1 to 20 A g^{-1}, about 82.1% retention rate of its initial value, indicating a high rate capability. Its rate capability and capacitance are the best among all the samples tested (Figure S12, Supporting Information), implying the importance of doping the proper amount of cobalt into the active material. Meanwhile, the corresponding areal capacitance for the sample with Ni:Co=5:5 is 2.0 F cm^{-2} at 4.6 mA cm^{-2} (Figure S13, Supporting Information). The Ni-Co@Ni-Co LDH NTAs/CFC reported here shows excellent electrochemical properties, compared with other nickel-cobalt composites reported (Table S2, Supporting

Information). The excellent properties are resulted from the improved charge transfer due to the increased electrical conductivity, the increased number of electroactive sites due to possible valence interchange or charge hopping between Ni and Co cations,[36] and the porous core-shell structure developed in the separated NTAs. The specific surface area is 112.2 $m^2 g^{-1}$ for the sample with Ni:Co=5:5 (Figure S14, Supporting Information).

Electrochemical impedance spectroscopy (EIS) (Figure 5f) shows that ESRs (equivalent series resistances) of the Ni-Co@Ni-Co LDH NTAs/CFC are about 1.43, 1.37, 1.19, 1.33 and 1.46 Ω, for the Ni:Co ratio of 10:0, 7:3, 5:5, 3:7, and 0:10, respectively. The small ESR for Ni-Co@Ni-Co LDH NTAs/CFC indicates low electrolyte resistance and low contact resistance between active material and the current collector. The low frequency portion of the EIS is a straight line, representing the Warburg resistance, which is related to ion diffusion/migration in the electrolyte. The sample of Ni:Co=5:5 shows a line with a higher slope than other ones, indicating faster ion diffusion between the electrode and the electrolyte. This result is in agreement with its higher specific capacitance and better rate capability. The cycling performance of the Ni-Co@Ni-Co LDH NTAs/CFC (Ni:Co=5:5) (Figure 5g) shows that, at a current density of 5 A g^{-1}, 98.8% of the initial capacitance (2200 F g^{-1}) is maintained after 5,000 cycles, also better than other compositions. Its morphology remains almost unchanged after 5,000 cycles, revealing an impressive structural stability (Figure S15, Supporting Information).

2.2 Battery-Type Supercapacitors

An all-solid-state flexible battery-type supercapacitor (FBSC) with KOH-PVA gel electrolyte was assembled using the as-prepared Ni-Co@Ni-Co LDH NTAs/CFC as the positive electrode and CNFs/CFC as the negative electrode (more information on the

CNFs/CFC electrode can be found from Supporting Information). To optimize the FBSC device capacitance with a stable potential window, CV curves of the two electrodes were separately measured at a scan rate of 10 mV s^{-1} (**Figure 6**a**)**. The mass loading on each electrode was determined according to the charge balance, i.e., $Q^{+} = Q^{-}$ and $Q^{\pm} = m^{\pm} C^{\pm} \Delta V^{\pm}$, where Q is the charge (C), m is the mass loading (g), C is the specific capacitance (F g^{-1}), ΔV it the voltage window (V) during charge/discharge process, and the superscripts + and – represent positive and negative electrodes, respectively.

Figure 6b shows the CV curves of an optimized FBSC at different cell voltages. The presence of the redox peaks is due to the Faradaic reactions of Ni-Co LDHs. With increasing cell voltage, the energy stored is also increased. As expected, a stable cell voltage window of the FBSC can be extended to 1.7 V.

Figure 7a shows the CV curves of an optimized FBSC at different scan rates from 5 to 100 mV s^{-1} between 0 and 1.7 V. There was no obvious shape change in the CV curves, indicating a good rate capability of the assembled device. The specific capacitance of the FBSC calculated based on the GCD curves (Figure 7b) reached 319 F g^{-1} at the current density of 2 A g^{-1}, much higher than many flexible supercapacitors reported previously (Table S3, Supporting Information). At higher discharge current densities of 5, 10, and 20 A g^{-1}, the device still delivers high specific capacitance of 280, 253, and 220 F g^{-1}, respectively (Figure 7c). The specific capacitance decreases with increasing current density, due to the incomplete redox reaction caused by sluggish ion diffusion at high current densities.[17a] The cycling life of the as-prepared FBSC was investigated by GCD measurement between 0 to 1.5 V at a current density of 5 A g^{-1} (Figure 7d). Interestingly, the capacitance was first deceased in the initial 200 cycles which may be caused by

inadequate wetting between the active material and the gel electrolyte. In the following GCD cycles, the capacitance rose again, which was probably due to the activation of active material and increased contact between the active material and the electrolyte. After 3,000 cycles, the FBSC showed a capacitance retention rate of 96.9%, demonstrating good cycling performance. This result is much better than those flexible devices reported in the literature (Table S4, Supporting Information).

The as-assembled FBSC was subject to a 90° bending test. **Figure 8**a shows that there was almost no change in CV curves before and after the bending, suggesting the good flexibility of the device. As a demonstration for practical application in energy storage, a red light-emitting diode (LED, 1.5 V) was lit up by two FBSCs connected in series (Figure 8b). GCD measurement (Figure 8c) shows that the discharge time of devices connected in parallel is twice as long as that of a single one within the same voltage window of 1.5 V. Meanwhile, the output voltage of devices connected in series is twice as high as that of a single one. These results reveal that the fabricated devices have good reproducibility and can be well managed for practical power applications.

Figure 8d shows the Ragone plot of our device in comparison with those state-of-the-art reported ones. Our device shows a maximum gravimetric energy density of 100 W h kg^{-1} at a power density of 1500 W kg^{-1}, which still remains a high enough value of 69 W h kg^{-1} at a high power density of 15 kW kg^{-1}. These values are higher than those devices reported recently, such as $Ni(OH)_2$/graphene||graphene (<78 W h kg^{-1}, <15 kW kg^{-1}),[13] $Ni(OH)_2$/CF||CNT/CF (<45 W h kg^{-1}, <3.5 kW kg^{-1}),[17c] $Co(OH)_xCO_3$/CF||CNT/CF (<35 W h kg^{-1}, <3.5 kW kg^{-1}),[17c] MnO_2-CNF||Bi_2O_3-CNF (12 W h kg^{-1}, <3.4 kW kg^{-1}),[37] Co_3O_4/VAGN/CF||Co_3O_4/VAGN/CF (<49 W h

kg^{-1}, <10 kW kg^{-1}),[17a] CNTG||MG (< 23 W h kg^{-1}, <9 kW kg^{-1}) [38], MnO_2/ACT||ACT(<67 W h kg^{-1}, <5 kW kg^{-1}).[39]

We attribute the excellent electrochemical performance of the assembled FBSC to the unique structural features of the positive electrode, Ni-Co@Ni-Co LDH NTAs/CFC. The well-aligned and separated nanotubes with massive hierarchical active material on the top provide a large amount of electrochemical active sites. The metallic core of the nanotubes transfers electrons efficiently from the massive top to the current collector on the bottom. Meanwhile, a proper mixture of Ni and Co optimizes the electrochemical properties of the electrode due to the synergistic effect between Ni and Co HDs.

3. Conclusion

An asymmetric battery-type supercapacitor using Ni-Co@Ni-Co LDH NTAs/CFC and CNFs/CFC as the positive and negative electrodes, respectively, was fabricated. The assembled device shows good flexibility, high energy density (100 W h kg^{-1} at 1500 W kg^{-1}) and good cycling stability (96.9% after 3,000 cycles) at a voltage window of 1.5 V, which are comparable to, or better than many of the state-of-the-art devices reported recently. The attractive properties are resulted from the unique structural features of the positive electrode, such as the metallic Ni/Co core inside the Ni-Co LDH nanotubes and massive active material on the top of nanotube array. The work presented here shows a good example of the combination of the electrode structural design and composition optimization for supercapacitor applications.

4. Experimental Section

Materials: All chemicals were of analytical grade and used as received without further purification. Electrodeposition was carried out in a two-electrode electrolytic cell by

galvanostatic electrodeposition. Platinum plate was used as the counter electrode (1cm×5cm) and the commercial CFC (WSO1002) was utilized as the working electrode (1cm×5cm).

Preparation of ZnO NRAs on CFC: ZnO NRAs were grown on CFC by electrodeposition in the solution of 1 mmol L^{-1} $Zn(NO_3)_2$ and 5 mmol/L NH_4NO_3 at a current density of 0.8 mA cm^{-2} for 1.5 h at 75 °C. During the electrodeposition process, the electrolytic cell was kept sealed to avoid water evaporation. After the deposition, CFC appeared white with the coating. As-deposited CFC was then washed thoroughly by deionized water and ethanol.

Preparation of Ni-Co@Ni-Co LDH NRAs on ZnO: Ni-Co@Ni-Co LDH NRAs were fabricated by electrodeposition of Ni-Co LDHs on the ZnO NRA-coated CFC under the optimized conditions (Figure S18, Supporting Information), with a current density of 4 mA cm^{-2} at 50 °C for 1.5 h. The electrolyte was 60 mL of a total of 2 mM metal ion solution ($NiSO_4·6H_2O$ and $CoSO_4·7H_2O$), with various Ni^{2+}/Co^{2+} feeding concentration ratios of 10:0, 7:3, 5:5, 3:7 and 0:10, containing 5 mM sodium dihydrogen citrate. The deposited CFC appeared black and was rinsed with deionized water and ethanol for several times. Finally, the obtained materials were dried at 60°C for 24 h. For comparison, *Ni-Co@Ni-Co LDHs/CFC* without ZnO template (Ni:Co=5:5) was prepared based on above process.

Preparation of Ni-Co@Ni-Co LDH NTAs on CFC: The ZnO NRA template was completely removed by immersing the sample in 1 mol L^{-1} NaOH for 6 h to produce Ni-Co@Ni-Co LDH NTAs/CFC.

Preparation of $MgCO_3/Ni(Ac)_2/PAN$ suspension: 1.0 g $MgCO_3 \cdot 3H_2O$ and 0.2 g $Ni(Ac)_2 \cdot 4H_2O$ were added in 10 mL DMF. After stirring for 2 h, a dispersed suspension was obtained. Meanwhile, 1.9 g PAN was dissolved in 10 mL DMF at 70°C with continuous stirring for 1 h. The suspension was then transferred to PAN solution with vigorous stirring for 3 h. Finally, the $MgCO_3/Ni(Ac)_2$/PAN suspension was obtained.

Electrospinning of $MgCO_3/Ni(Ac)_2/PAN$ suspension: the suspension was spun into nanofibers using electrospinning. In a typical process, the suspension was loaded into a 20 mL plastic syringe with a stainless steel pinhead connected with a 17 kV DC supply, and extruded at room temperature in air at a feeding rate of 0.06 mm min^{-1}. A distance of 20 cm was kept between the needle tip and the aluminum foil collector.

Preparation of CNFs: The $MgCO_3/Ni(Ac)_2$/PAN nanofibers were firstly dried at 60°C for 3 h, and then annealed at 250°C for 2 h in air for composite stabilization. Subsequently, carbonization was carried out at 450°C for 1 h and 800°C for 3 h in N_2 to obtain MgO/Ni/carbon nanofiber with a heating rate of 5°C min^{-1}. After that, a mixture of MgO/Ni/carbon nanofiber with KOH was added into 200 ml deionized water followed by vigorous stirring at 120°C until the formation of a slurry. The slurry was then calcined at 250°C for 30 min and 750°C for 1 h in a tube furnace under N_2 atmosphere with a heating rate of 5°C min^{-1}. Finally, the as-obtained product was further treated using diluted HNO_3 solution to remove Ni, MgO and KOH, then filtrated and washed with deionized water until the filtrate became neutral. CNFs were obtained after subsequent drying at 60°C for 12 h.

Preparation of CNFs on the CFC: a slurry was obtained by mixing carbon nanofibers (as the active material), with acetylene black (as conductive agent) and

polyvinylidene fluoride (as the binder) in a mass ratio of 80:10:10 in 1-methyl-2-pyrrolidinone. The paste was then pressed onto carbon fiber cloth (1cm×3 cm) and dried at 80°C for 24 h.

Preparation of PVA-KOH gel electrolyte: PVA-KOH gel electrolyte was prepared using PVA (molecular weight: 6450 g mol^{-1}) and KOH. Firstly, 2 g PVA was dissolved in 20 mL deionized water by continuous stirring and kept at 90°C for 2 h until a clear viscous solution was obtained. When it was cooled down, 2g of concentrated KOH solution was added to the viscous solution slowly under stirring until a clear solution was prepared.

Fabrication of solid-state flexible supercapacitor: The as-prepared Ni-Co@Ni-Co LDH NTAs/CFC and CNFs/CFC were soaked into the hot PVA-KOH gel electrolyte (50~60°C) for 10 min and hung for 15 min under ambient condition to allow the electrolyte to diffuse into the nanoporous structure of active materials. This coating process was repeated three times. Then the two electrodes were pressed against each other and dried in hot air until the gel electrolyte was solidified and the deionized water evaporated. Silver paste was used for electric contact between CFC and instrument. The as-fabricated battery-type supercapacitor is labeled as Ni-Co@Ni-Co LDH NTAs/CFC||CNFs/CFC.

Characterization: Scanning Electron Microscope (SEM, TM 3000, Hetachi, Japan) and Transmission Electron Microscope (TEM, JOEL JEM-2010, Japan) were used for microstructure and morphology characterizations. X-ray diffraction (XRD, Rigaku D/max IIIA, Cu kα, λ=0.15418 nm, Japan) was performed for crystalline structure analysis. Raman spectra were taken on a HORIBA HR800 Raman spectrometer at 488

nm. X-ray photoelectron spectroscopy (XPS, Thermo Microlab 350) was employed to study the surface composition of Ni-Co hybrid NTAs inside an ultrahigh vacuum system. Depth profile XPS was used to analyze the elemental distribution of the core-shell structure of Ni-Co@Ni-Co LDH NTAs deposited on a Ni foil, along the direction perpendicular to the substrate. The sample was etched at a rate of 3 nm/min by Ar^+ ions. N_2 adsorption/desorption isotherms were measured at 77 K (liquid nitrogen) with a Micromeritics ASAP2020 volumetric adsorption analyzer.

Electrochemical Measurement: Cyclic voltammetry (CV) curves, galvanostatic charge/discharge (GCD) and electrochemical impedance spectroscopy (EIS, 5 mV amplitude 0.01~10k Hz frequency) tests were recorded by CHI660e (Chenhua, China) with a classical three-electrode configuration (platinum as counter electrode and saturated calomel as reference electrode) in 1 mol L^{-1} NaOH. CV curves were measured between -0.2 and 0.65 V at different scan rates. GCD tests were carried out from 0 to 0.5 V at different current densities. The mass densities of the active materials loaded on the electrodes are 0.87~0.91 mg cm^{-2}.

Acknowledgements:

This work was supported by the Research Grants Council of the Hong Kong Special Administrative Region, China (Project Nos. M-PolyU503/13 and PolyU5159/13E) and Hong Kong Polytechnic University (Project Nos. 1-BBA3 and 1-ZVGH).

References

[1] P. Simon; Y. Gogotsi, Nat. Mater. 7 (2008) 845-854.

[2] E. S. Snow; F. K. Perkins; E. J. Houser; S. C. Badescu; T. L. Reinecke, Science 307 (2005) 1942-1945.

[3] H. Nakagawa; A. Shudo; K. Miura, J. Electrochem. Soc. 147 (2000) 38-42.

[4] a) J. R. Miller; R. A. Outlaw, J. Electrochem. Soc. 162 (2015) A5077-A5082; b) J. R. Miller; R. A. Outlaw; B. C. Holloway, Science 329 (2010) 1637-1639.

[5] J. H. Kim; D. S. Kil; S. J. Yeom; J. S. Roh; N. J. Kwak; J. W. Kim, Appl. Phys. Lett. 91 (2007) 052908-052911.

[6] Q. Li; Z.-L. Wang; G.-R. Li; R. Guo; L.-X. Ding; Y.-X. Tong, Nano Lett. 12 (2012) 3803-3807.

[7] S. K. Meher; G. R. Rao, J. Phys. Chem. C 115 (2011) 15646-15654.

[8] a) H. Wang; H. S. Casalongue; Y. Liang; H. Dai, J. Am. Chem. Soc. 132 (2010) 7472-7477; b) X. Dong; Z. Guo; Y. Song; M. Hou; J. Wang; Y. Wang; Y. Xia, Adv. Funct. Mater. 24 (2014) 3405-3412.

[9] U. M. Patil; M. S. Nam; J. S. Sohn; S. B. Kulkarni; R. Shin; S. Kang; S. Lee; J. H. Kim; S. C. Jun, J. Mater. Chem. A 2 (2014) 19075-19083.

[10] A. Yoshizawa; M. Takeda; Y. Oura; Y. Takemoto; K. Naoi, Electrochemistry 67 (1999) 45-50.

[11] B. C. Kim; J. M. Ko; G. G. Wallace, J. Power Sources 177 (2008) 665-668.

[12] a) Z. Tang; C. H. Tang; H. Gong, Adv. Funct. Mater. 22 (2012) 1272-1278; b) H. Jiang; C. Z. Li; T. Sun; J. Ma, Chem. Commun. 48 (2012) 2606-2608; c) H. T.

Zhang; X. Zhang; D. C. Zhang; X. Z. Sun; H. Lin; C. H. Wang; Y. W. Ma, J. Phys. Chem. B 117 (2013) 1616-1627; d) R. R. Salunkhe; J. J. Lin; V. Malgras; S. X. Dou; J. H. Kim; Y. Yamauchi, Nano Energy 11 (2015) 211-218; e) H. B. Wu; H. Pang; X. W. Lou, Energy Environ. Sci. 6 (2013) 3619-3626; f) L. Huang; D. Chen; Y. Ding; S. Feng; Z. L. Wang; M. Liu, Nano Lett. 13 (2013) 3135-3139.

[13] J. Yan; Z. Fan; W. Sun; G. Ning; T. Wei; Q. Zhang; R. Zhang; L. Zhi; F. Wei, Adv. Funct. Mater. 22 (2012) 2632-2641.

[14] H. Chen; L. Hu; M. Chen; Y. Yan; L. Wu, Adv. Funct. Mater. 24 (2014) 934-942.

[15] Y. Cheng; H. Zhang; C. V. Varanasi; J. Liu, Energy Environ. Sci. 6 (2013) 3314-3321.

[16] a) Y. K. Hsu; Y. C. Chen; Y. G. Lin; L. C. Chen; K. H. Chen, J. Mater. Chem. 22 (2012) 3383-3387; b) K. Y. Shi; I. Zhitomirsky, Chemelectrochem 2 (2015) 396-403; c) S. T. Senthilkumar; R. K. Selvan; N. Ponpandian; J. S. Melo; Y. S. Lee, J. Mater. Chem. A 1 (2013) 7913-7919; d) A. Pramanik; S. Maiti; S. Mahanty, Dalton Transactions (2015) 14604-14612; e) X. Du; C. Wang; M. Chen; Y. Jiao; J. Wang, J. Phys. Chem. C 113 (2009) 2643-2646; f) A. Balducci; R. Dugas; P. L. Taberna; P. Simon; D. Plée; M. Mastragostino; S. Passerini, J. Power Sources 165 (2007) 922-927; g) T. Y. Kim; H. W. Lee; M. Stoller; D. R. Dreyer; C. W. Bielawski; R. S. Ruoff; K. S. Suh, ACS nano 5 (2010) 436-442.

[17] a) Q. Y. Liao; N. Li; S. X. Jin; G. W. Yang; C. X. Wang, ACS Nano 9 (2015) 5310-5317; b) L. Yuan; X.-H. Lu; X. Xiao; T. Zhai; J. Dai; F. Zhang; B. Hu; X.

Wang; L. Gong; J. Chen; C. Hu; Y. Tong; J. Zhou; Z. L. Wang, ACS Nano 6 (2012) 656-661; c) D. Ghosh; M. Mandal; C. K. Das, Langmuir (2015) 7835-7843.

[18] A. Izadi-Najafabadi; D. N. Futaba; S. Iijima; K. Hata, J. Am. Chem. Soc. 132 (2010) 18017-18019.

[19] Q. Li; C.-L. Liang; X.-F. Lu; Y.-X. Tong; G.-R. Li, J. Mater. Chem. A 3 (2015) 6432-6439.

[20] a) X.-F. Lu; J. Lin; Z.-X. Huang; G.-R. Li, Electrochim. Acta 161 (2015) 236-244; b) Z.-L. Wang; R. Guo; G.-R. Li; H.-L. Lu; Z.-Q. Liu; F.-M. Xiao; M. Zhang; Y.-X. Tong, J. Mater. Chem. 22 (2012) 2401-2404.

[21] a) X. Yin; C. Tang; L. Zhang; Z. G. Yu; H. Gong, Sci. Rep. 6 (2016) 21566-21577; b) X. Li; J. Shen; W. Sun; X. Hong; R. Wang; X. Zhao; X. Yan, J. Mater. Chem. A 3 (2015) 13244-13253.

[22] R. Li; S. Wang; Z. Huang; F. Lu; T. He, J. Power Sources 312 (2016) 156-164.

[23] C.-h. Tang; X. Yin; H. Gong, ACS Appl. Mater. Interfaces 5 (2013) 10574-10582.

[24] Y. Liu; N. Fu; G. Zhang; W. Lu; L. Zhou; H. Huang, J. Mater. Chem. A 4 (2016) 15049-15056.

[25] Z. Yin; S. Wu; X. Zhou; X. Huang; Q. Zhang; F. Boey; H. Zhang, Small 6 (2010) 307-312.

[26] W. Yan; D. Wang; G. G. Botte, Electrochim. Acta 61 (2012) 25-30.

[27] a) M. A. Sayeed; T. Herd; A. P. O'Mullane, J. Mater. Chem. A 4 (2016) 991-999; b) J. Yang; H. Liu; W. N. Martens; R. L. Frost, J. Phys. Chem. C 114 (2010) 111-119.

[28] S. Deabate; F. Fourgeot; F. Henn, J. Power Sources 87 (2000) 125-136.

[29] C. Zhang; J. Zhao; L. Zhou; Z. Li; M. Shao; M. Wei, J. Mater. Chem. A 4 (2016) 11516-11523.

[30] B. Santara; B. Pal; P. K. Giri, J. Appl. Phys. 110 (2011) 114322.

[31] O. Bøckman; T. Østvold; G. A. Voyiatzis; G. N. Papatheodorou, Hydrometallurgy 55 (2000) 93-105.

[32] H. B. Li; M. H. Yu; X. H. Lu; P. Liu; Y. Liang; J. Xiao; Y. X. Tong; G. W. Yang, ACS Appl. Mater. Interfaces 6 (2014) 745-749.

[33] X.-F. Lu; D.-J. Wu; R.-Z. Li; Q. Li; S.-H. Ye; Y.-X. Tong; G.-R. Li, J. Mater. Chem. A 2 (2014) 4706-4713.

[34] Y. Zhao; L. Hu; S. Zhao; L. Wu, Adv. Funct. Mater. 26 (2016) 4038-4038.

[35] a) X. Zheng; Z. Gu; Q. Hu; B. Geng; X. Zhang, RSC Advances 5 (2015) 17007-17013; b) R. R. Salunkhe; K. Jang; S.-w. Lee; H. Ahn, RSC Advances 2 (2012) 3190-3193.

[36] a) X. Liu; R. Ma; Y. Bando; T. Sasaki, Adv. Mater. 24 (2012) 2148-2153; b) V. Gupta; S. Gupta; N. Miura, J. Power Sources 175 (2008) 680-685; c) R. D. Armstrong; E. A. Charles, J. Power Sources 25 (1989) 89-97.

[37] H. H. Xu; X. L. Hu; H. L. Yang; Y. M. Sun; C. C. Hu; Y. H. Huang, Adv. Energy Mater. 5 (2015) 1401882-1401888.

[38] H. Gao; F. Xiao; C. B. Ching; H. Duan, ACS Appl. Mater. Interfaces 4 (2012) 7020-7026.

[39] L. Bao; X. Li, Adv. Mater. 24 (2012) 3246-3252.

Hierarchical nickel-cobalt@nickel-cobalt layered double hydroxide nanotube arrays with separated tubes and massive top are designed and fabricated by facile electrodeposition. The as-prepared electrode possesses numerous electroactive sites, a highly conductive Ni/Co metallic core, and a high capacitance Ni-Co layered double hydroxide shell. The assembled battery-type supercapacitor exhibits superior gravimetric capacitance, good rate performance, high specific energy and high power density.

Keywords: Hierarchical porous nanotubes; Electrode; Ni-Co@Ni-Co LDH core-shell structure; battery-type supercapacitor.

*Yan Liu, Nianqing Fu, Guoge Zhang, Ming Xu, Wei Lu, Limin Zhou, Haitao Huang**

Design of Hierarchical Ni-Co@Ni-Co Layered Double Hydroxide Core-Shell Structured Nanotube Array for High-Performance Flexible All-Solid-State Battery-type Supercapacitors

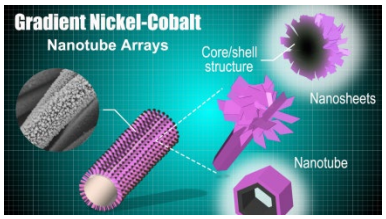

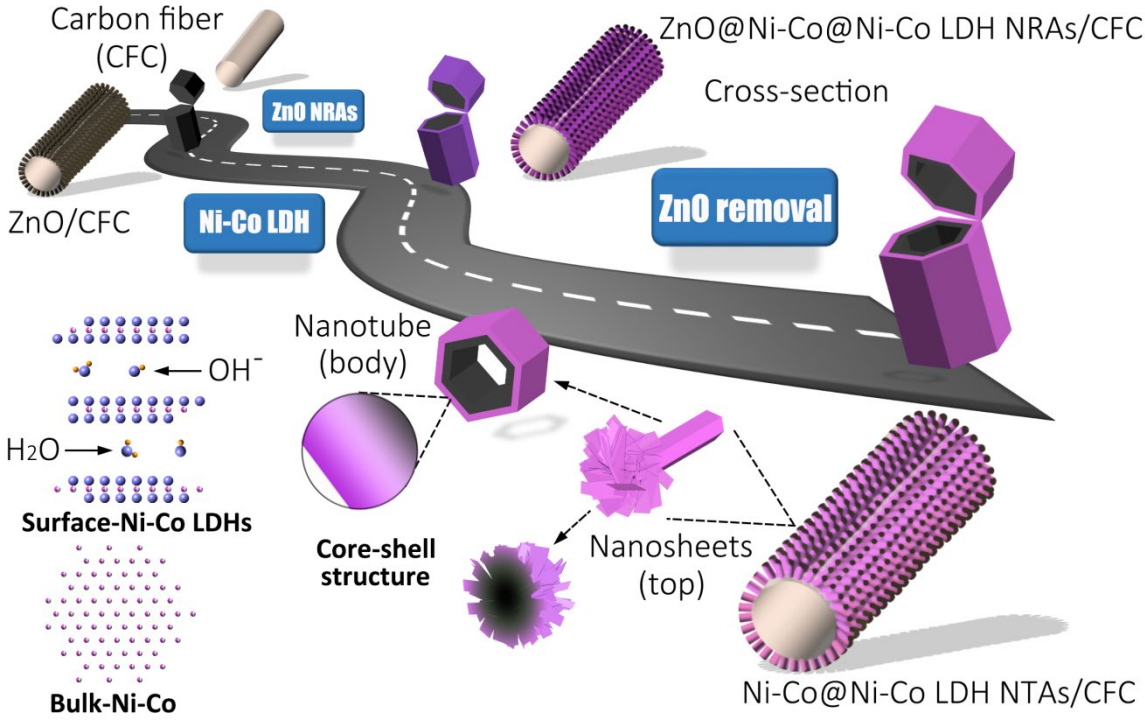

Scheme 1. Schematic diagram of the preparation procedures of the hierarchically porous Ni-Co@Ni-Co LDH NTAs on CFC.

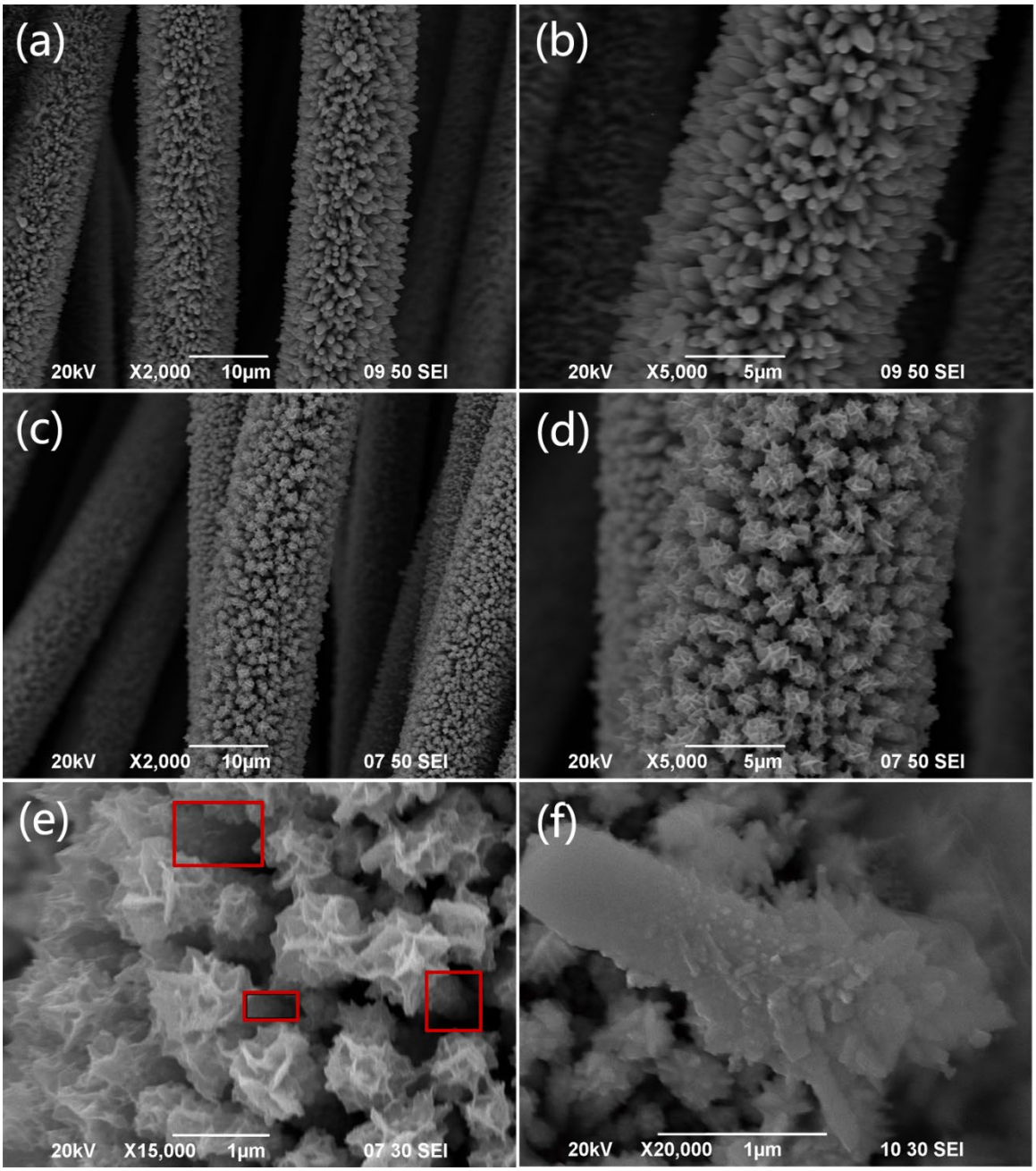

Figure 1. SEM images. (a, b) ZnO NRAs, (c, d, e) Ni-Co@Ni-Co LDH NRAs on ZnO template and (f) a single Ni-Co@Ni-Co LDH NR grown on a ZnO NR by electrodeposition. Ni:Co=5:5.

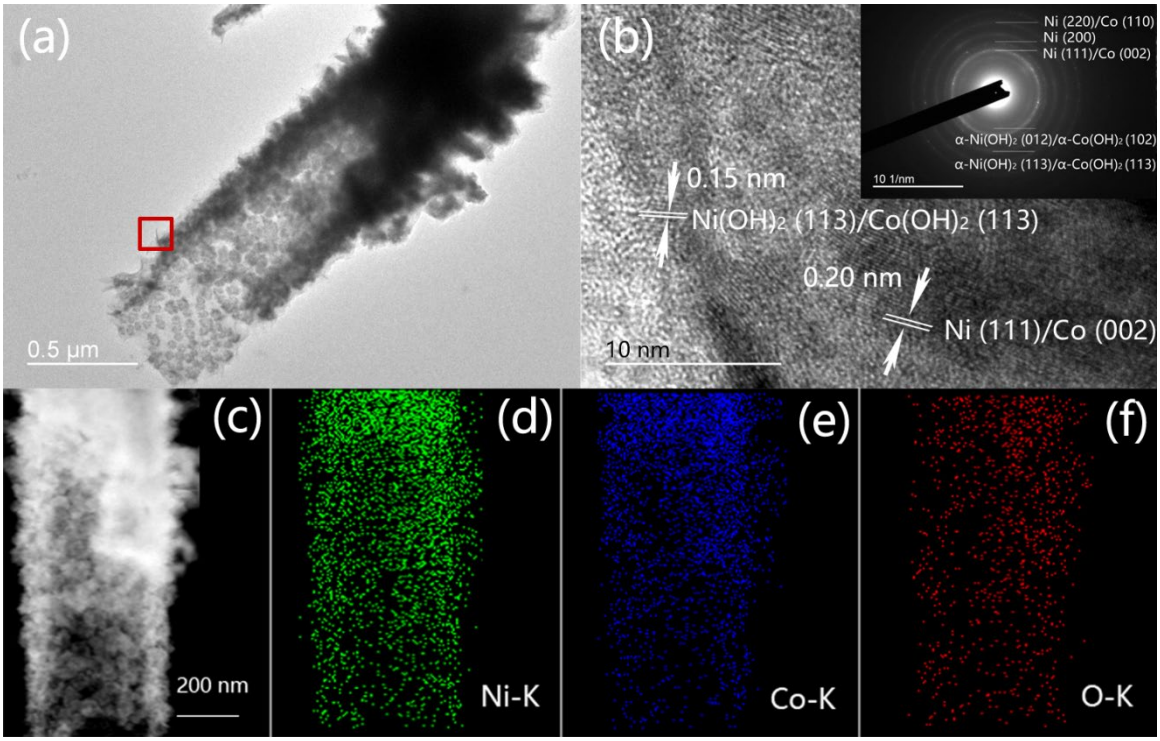

Figure 2. Body of the Ni-Co@Ni-Co LDH NTAs (Ni:Co=5:5): (a) TEM image, (b) HRTEM image and SAED pattern (inset) of the selected area in (a), (c) STEM bright field image, and (d-f) elemental mapping of Ni, Co and O.

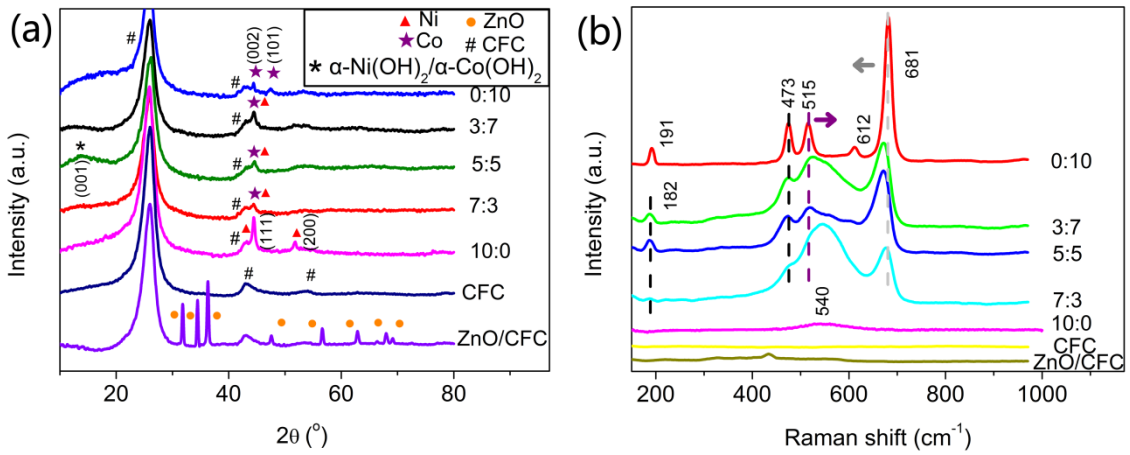

Figure 3. (a) XRD patterns and (b) Raman spectra of CFC, ZnO and Ni-Co@Ni-Co LDH NTAs/CFC with different Ni:Co ratios.

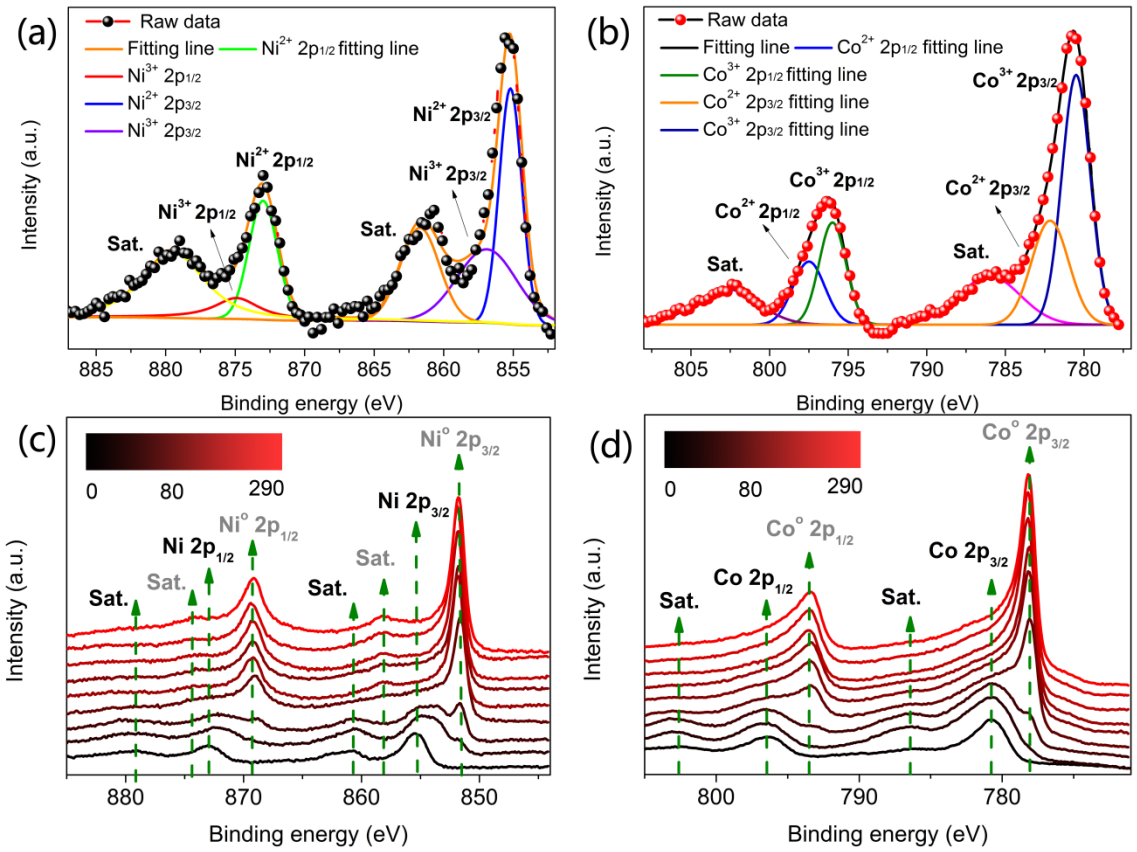

Figure 4. (a) Ni 2p XPS, (b) Co 2p XPS, (c) depth profile of Ni 2p XPS, and (d) depth profile of Co 2p XPS of the as-obtained Ni-Co@Ni-Co LDH NTAs/CFC (Ni:Co=5:5). Etching depth is from 0 to 290 nm.

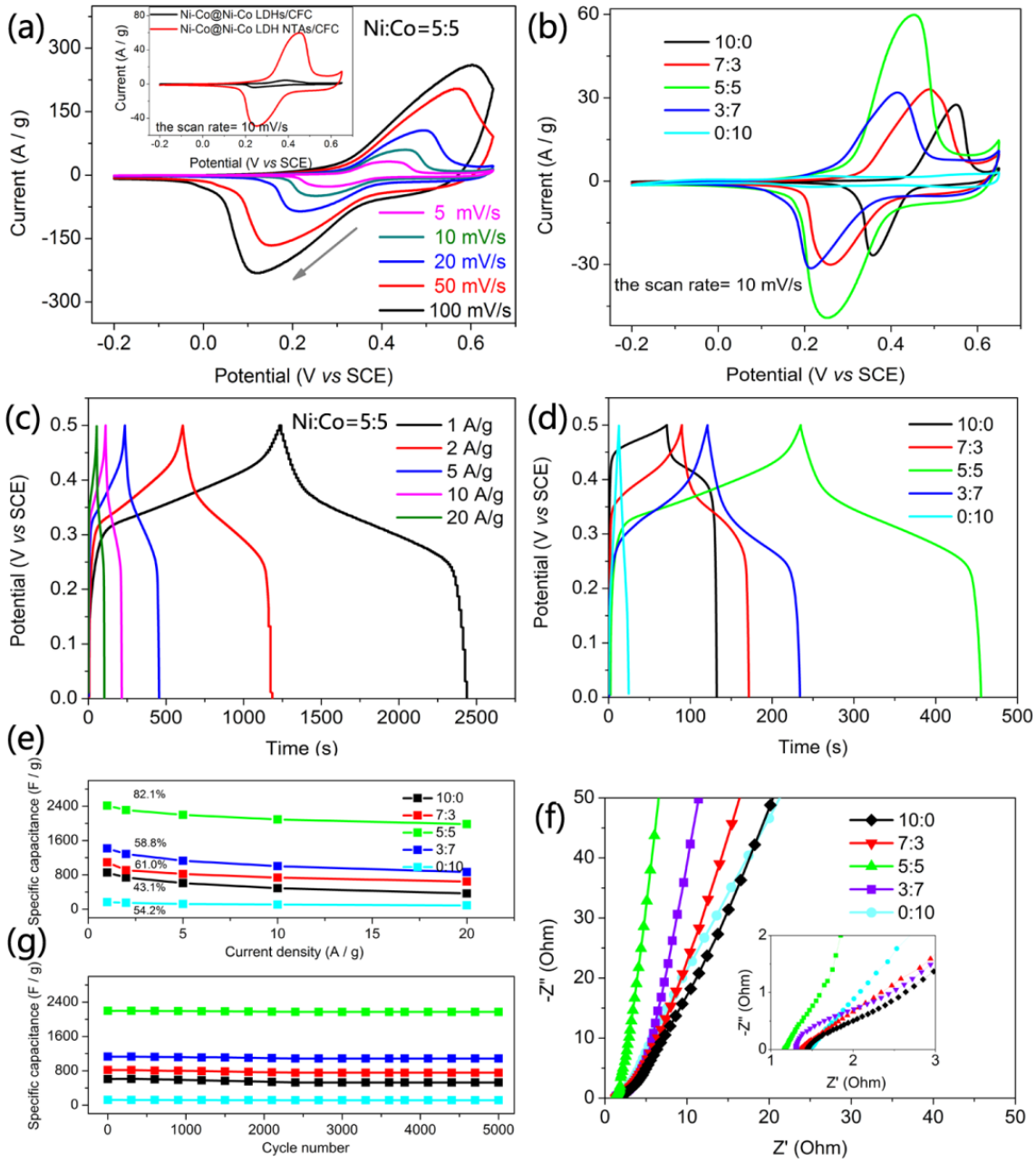

Figure 5. Electrochemical properties of Ni-Co@Ni-Co LDH NTAs/CFC (a) CVs of the Ni:Co=5:5 sample. Inset: CVs of Ni-Co@Ni-Co LDH NTAs/CFC and Ni-Co LDHs/CFC at a scan rate of 10 mV s^{-1}. (b) CVs of samples of different Ni:Co ratios. (c) GCD curves of the Ni:Co=5:5 sample. (d) GCD curves of samples with different Ni:Co ratios at a current density of 5 A g^{-1}. (e) Specific capacitance *vs*. current density. (f) Nyquist plots.

Inset: magnified EIS spectra at the high frequency region. (g) Cycling performance at a current density of 5 A g^{-1}.

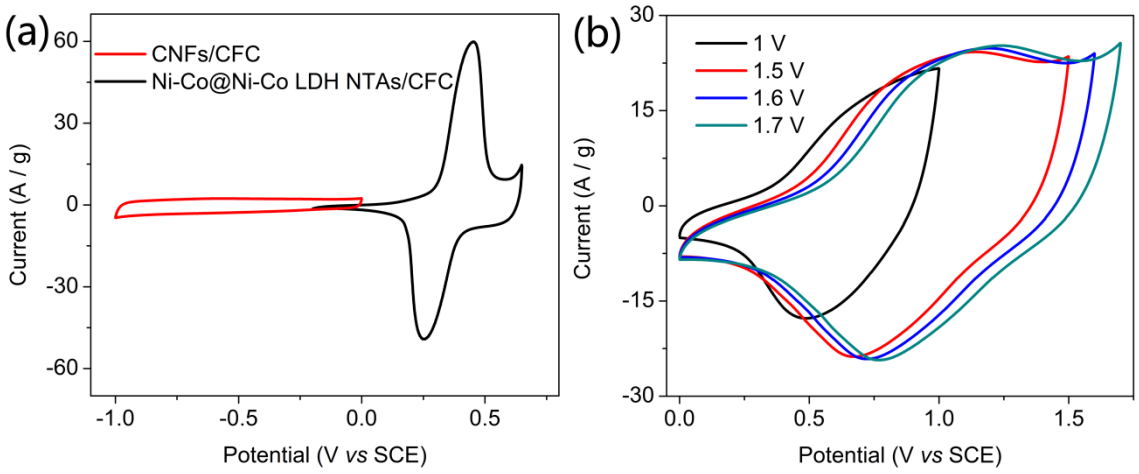

Figure 6. CV curves of (a) Ni-Co@Ni-Co LDH NTAs/CFC and CNFs/CFC electrodes at a scan rate of 10 mV s^{-1}, and (b) an optimized FBSC device in various voltage windows at a scan rate of 100 mV s^{-1}.

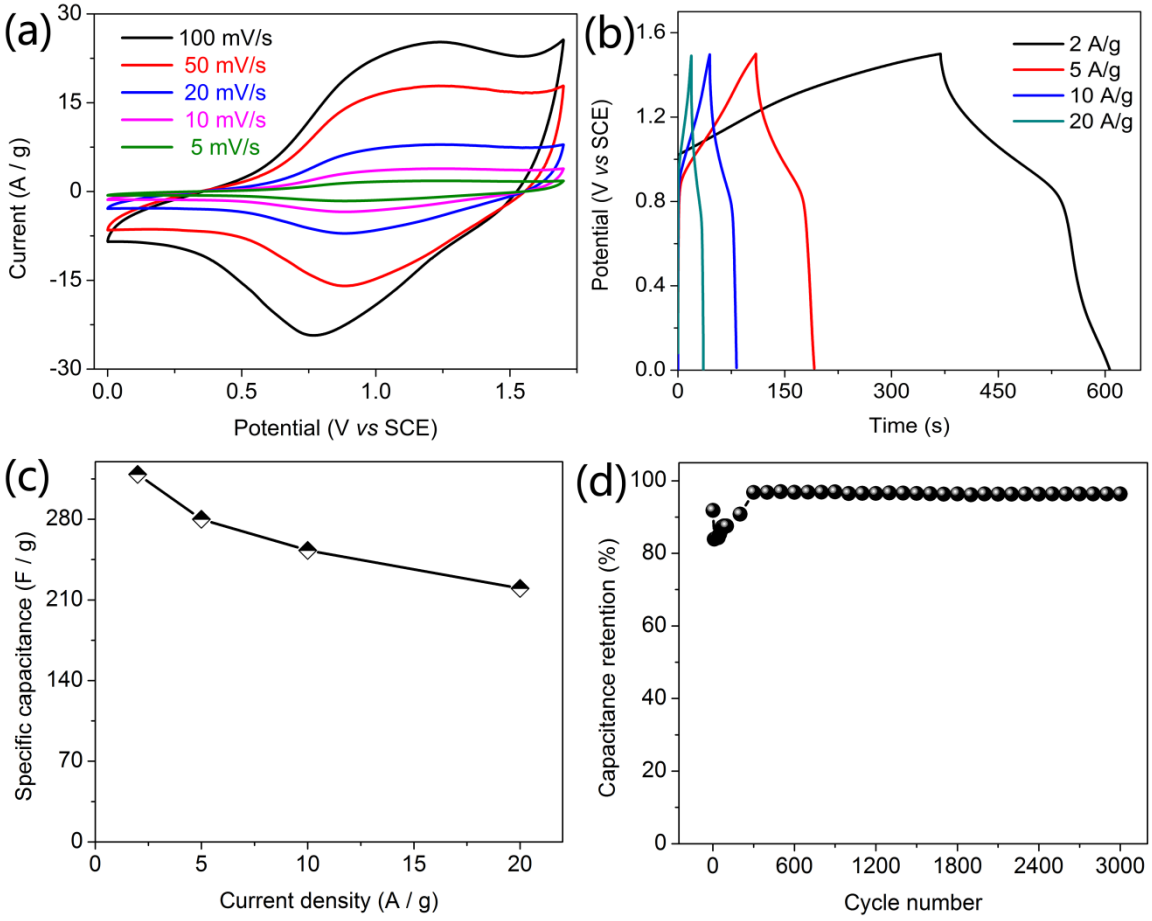

Figure 7. (a) CVs at different scan rates, (b) GCD curves at different current densities, (c) specific capacitance at different current densities, and (d) Cycling performance at a current density of 5 A g^{-1} of an optimized FBSC device.

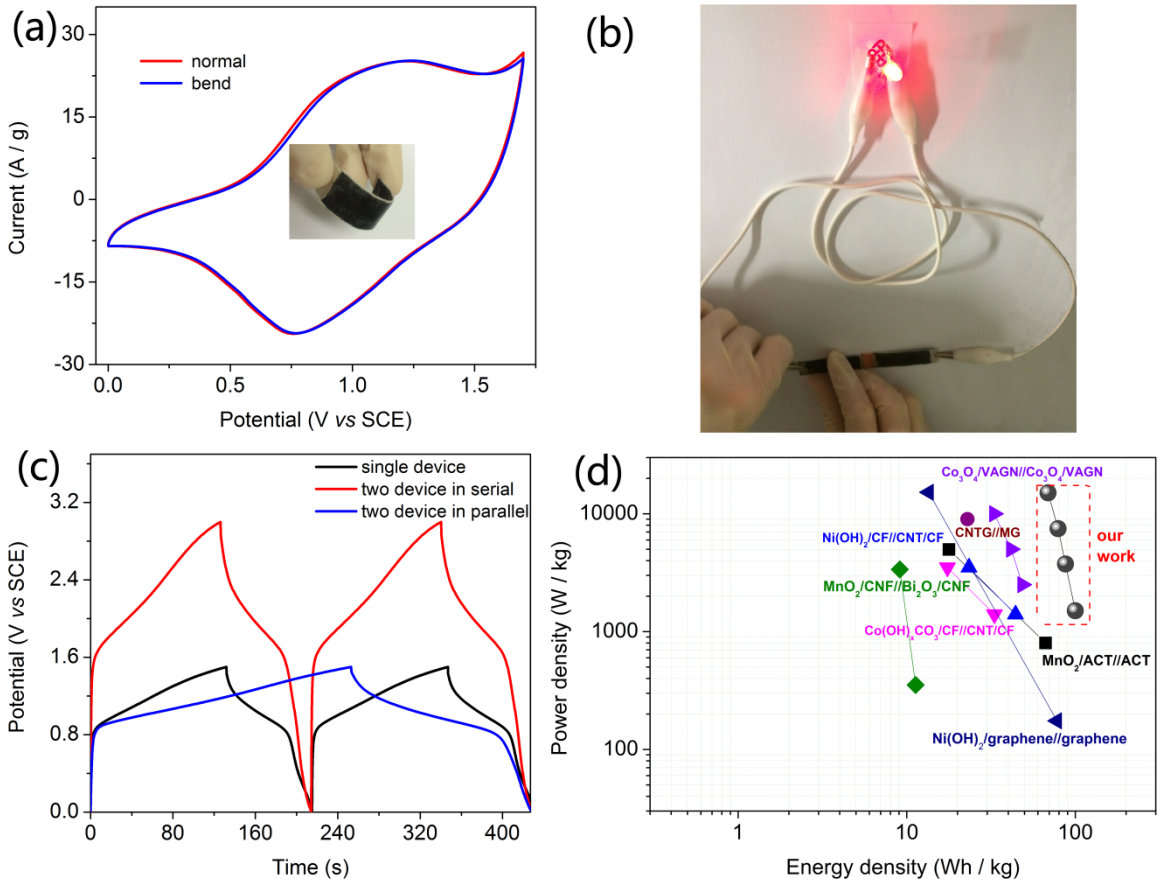

Figure 8. (a) CVs of the FBSC device under flat and bending conditions at a scan rate of 100 mV s^{-1}. Inset: digital image of a 90° bended device. (b) Digital image of a LED lit up by two tandem devices. (c) GCD curves of two FBSCs in series and in parallel at a current density of 5 A g^{-1}. A single device is also plotted for comparison. (d) Ragone plot of our device in comparison with those reported ones.